

# The role of diffuse electron precipitation in the formation of subauroral polarization streams

Dong Lin<sup>1</sup>, Kareem Sorathia<sup>2</sup>, Wenbin Wang<sup>3</sup>, Viacheslav G. Merkin<sup>4</sup>, Shanshan Bao<sup>5</sup>, Kevin H Pham<sup>1</sup>, Frank R. Toffoletto<sup>5</sup>, Xueling Shi<sup>6</sup>, Adam Michael<sup>7</sup>, John G. Lyon<sup>8</sup>, Jeffrey Garretson<sup>9</sup>, and Brian J. Anderson<sup>10</sup>

<sup>1</sup>National Center for Atmospheric Research

<sup>2</sup>Applied Physics Laboratory, Johns Hopkins University

<sup>3</sup>HAO/NCAR

<sup>4</sup>The Johns Hopkins University Applied Physics Laboratory

<sup>5</sup>Rice University

<sup>6</sup>Virginia Polytechnic Institute and State University

<sup>7</sup>John Hopkins Applied Physics Laboratory

<sup>8</sup>Dartmouth College

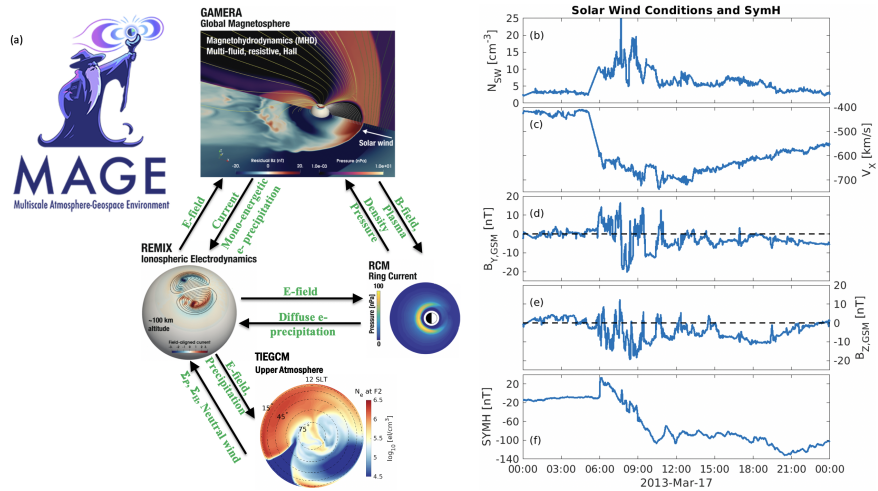
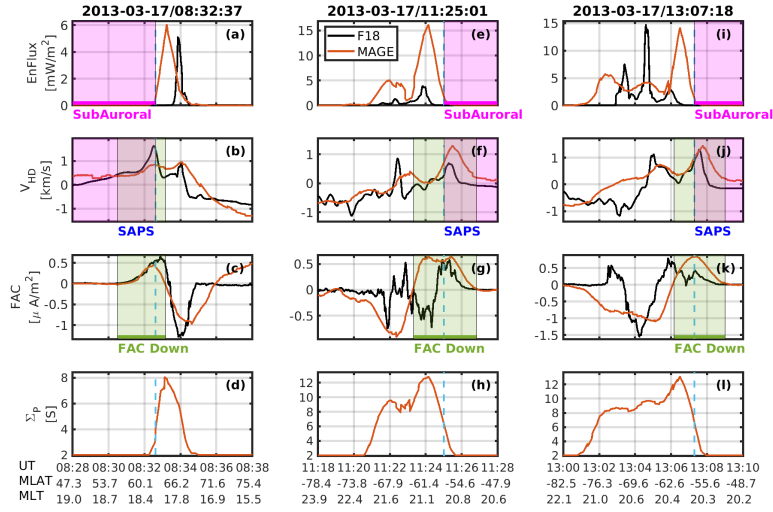
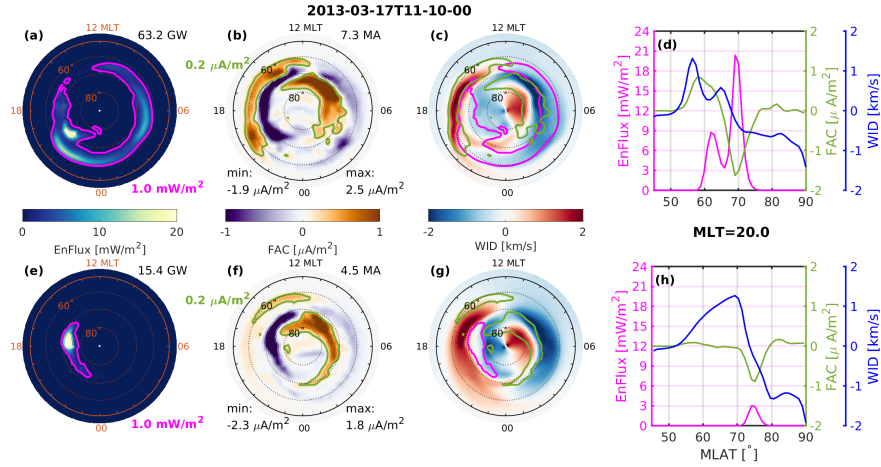
<sup>9</sup>Johns Hopkins Applied Physics Lab

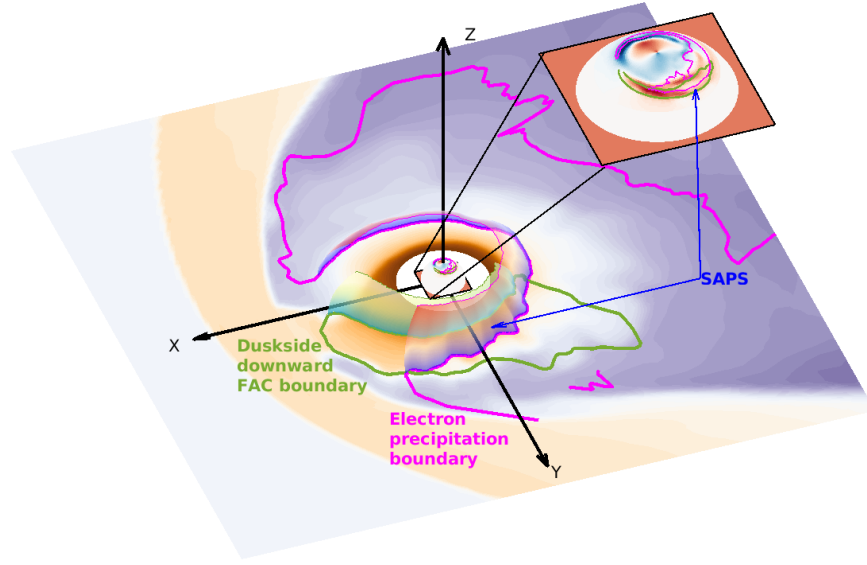
<sup>10</sup>John Hopkins Univ.

November 23, 2022

## Abstract

The role of diffuse electron precipitation in forming subauroral polarization streams (SAPS) is investigated with the Multiscale Atmosphere-Geospace Environment (MAGE) model. Diffuse precipitation is derived from the distribution of drifting electrons calculated in MAGE. SAPS manifest themselves as a separate mesoscale flow channel in the duskside ionosphere when diffuse precipitation is implemented in MAGE, whereas it merges with the primary auroral convection when diffuse precipitation is turned off. SAPS overlap with the downward Region-2 field-aligned currents equatorward of diffuse precipitation, where poleward electric fields closing the Pedersen currents are strong due to a low conductance in the subauroral ionosphere. The Region-2 field-aligned currents extend to lower latitudes than diffuse precipitation because the ring current protons penetrate closer to the Earth than the electrons do. This study demonstrates the critical role of diffuse electron precipitation in determining SAPS location and structure.





1                   **The role of diffuse electron precipitation in the**  
2                   **formation of subauroral polarization streams**

3                   **Dong Lin<sup>1</sup>, Kareem Sorathia<sup>2</sup>, Wenbin Wang<sup>1</sup>, Viacheslav Merkin<sup>2</sup>, Shanshan**  
4                   **Bao<sup>3</sup>, Kevin Pham<sup>1</sup>, Frank Toffoletto<sup>3</sup>, Xueling Shi<sup>4,1</sup>, Adam Michael<sup>2</sup>, John**  
5                   **Lyon<sup>5</sup>, Jeffrey Garretson<sup>2</sup>, and Brian Anderson<sup>2</sup>**

6                   <sup>1</sup>High Altitude Observatory, National Center for Atmospheric Research, Boulder CO

7                   <sup>2</sup>Applied Physics Laboratory, Johns Hopkins University, Laurel MD

8                   <sup>3</sup>Department of Physics and Astronomy, Rice University, Houston TX

9                   <sup>4</sup>Bradley Department of Electrical and Computer Engineering, Virginia Tech, Blacksburg VA

10                   <sup>5</sup>Department of Physics and Astronomy, Dartmouth College, Hanover NH

11                   **Key Points:**

- 12                   • Physics-based diffuse electron precipitation is implemented in a fully coupled magnetosphere-
- 13                   ionosphere-thermosphere model.
- 14                   • Diffuse electron precipitation plays a key role in determining the location and struc-
- 15                   ture of subauroral polarization streams.
- 16                   • Subauroral polarization streams form between the inner edges of the proton ring
- 17                   current and electron plasmashet.

**Abstract**

The role of diffuse electron precipitation in forming subauroral polarization streams (SAPS) is investigated with the Multiscale Atmosphere-Geospace Environment (MAGE) model. Diffuse precipitation is derived from the distribution of drifting electrons calculated in MAGE. SAPS manifest themselves as a separate mesoscale flow channel in the duskside ionosphere when diffuse precipitation is implemented in MAGE, whereas it merges with the primary auroral convection when diffuse precipitation is turned off. SAPS overlap with the downward Region-2 field-aligned currents equatorward of diffuse precipitation, where poleward electric fields closing the Pedersen currents are strong due to a low conductance in the subauroral ionosphere. The Region-2 field-aligned currents extend to lower latitudes than diffuse precipitation because the ring current protons penetrate closer to the Earth than the electrons do. This study demonstrates the critical role of diffuse electron precipitation in determining SAPS location and structure.

**Plain Language Summary**

[Subauroral polarization streams (SAPS) are a mesoscale ( $\sim 100$ - $500$  km) plasma flow channel frequently observed in the duskside subauroral ionosphere. This study investigates how diffuse electron precipitation affects the location and structure of SAPS, enabled by the newly developed model capability to directly simulate diffuse precipitation using particle drift physics in a state-of-the-art geospace model called MAGE. Numerical experiments show that SAPS are a separate flow channel when diffuse precipitation is included in the simulation, but they merge with the primary auroral convection when diffuse precipitation is off. SAPS are produced in the gap between the low latitude boundaries of electron aurora and downward field-aligned current (FAC) on the duskside, where the ionospheric conductance is low due to lack of ionization while substantial downward region-2 FAC requires closure. Strong poleward electric fields are generated to drive the enhanced westward ion drifts of SAPS. Tracing back to the magnetosphere, the gap between inner boundaries is formed because the ring current protons, whose distribution primarily determines the downward FAC, penetrate deeper than the electrons, the source population of diffuse precipitation. This study demonstrates the importance of including diffuse precipitation in coupled geospace models to understand the dynamics of mesoscale SAPS structures.]

**1 Introduction**

Auroral precipitation plays a significant role in the magnetosphere-ionosphere-thermosphere (MIT) coupling by enhancing ionospheric ionization and conductivity at high latitudes (e.g., Hardy et al., 1987). Since MIT electrodynamic coupling depends strongly on the ionospheric conductance (e.g., Hill et al., 1976; Southwood & Wolf, 1978; Foster et al., 1986; Merkin et al., 2003, 2005; Jensen et al., 2017), auroral precipitation affects global ionospheric plasma convection. Among the various types of auroral precipitation that have been identified from satellite measurements, diffuse electron precipitation is the most commonly detected and makes the largest contribution to the total precipitation budget (Newell et al., 2009). The statistical study of Newell et al. (2009) showed that diffuse precipitation contributes up to  $\sim 60\%$  of the total precipitation energy flux under both weak and strong solar wind driving conditions. The empirical orthogonal function analysis of McGranaghan et al. (2015) revealed that diffuse precipitation is responsible for the mean pattern and principle variability of ionospheric conductance. Therefore, the distribution of diffuse precipitation is expected to have important impacts on the ionospheric convection and MI coupling processes.

The subauroral polarization streams (SAPS) are mesoscale ( $\sim 100$  to  $500$  km at ionospheric altitudes) structures that are frequently observed in the duskside ionosphere. SAPS manifest themselves as a latitudinally narrow, high-speed, westward plasma flow chan-

nel ( $\sim 1$ -5 degrees) equatorward of the low latitude electron auroral boundary (e.g., Foster & Vo, 2002). Previous studies have shown that SAPS represent sophisticated MIT coupling processes that require synergistic investigations of the interactions between solar wind, outer and inner magnetosphere, and ionosphere-thermosphere (e.g., Ebihara et al., 2009; Wang et al., 2012; Califf et al., 2016; Kunduri et al., 2017; He et al., 2017; Yuan et al., 2017; Huang, 2020). Coupled geospace models provide a more comprehensive and self-consistent view of SAPS in the context of MIT coupling (e.g., Yu et al., 2015; Raeder et al., 2016; Lin et al., 2019) compared to empirical or prescribed specification of SAPS in standalone magnetospheric and ionospheric models (e.g., Zheng et al., 2008; Wang et al., 2012; Guo et al., 2018; Ferdousi et al., 2019). Although existing coupled geospace models provide overall reasonable representations of the global ionospheric convection pattern, it is still challenging for them to fully reproduce the physics of SAPS, particularly at mesoscales. For example, Lin et al. (2019) used a coupled MIT model to simulate SAPS during the 17 March 2013 geomagnetic storm. The SAPS channel was not discernible from the auroral convection compared with Defense Meteorology Satellite Program (DMSP) measurements, which was attributed to the lack of a faithful representation of the diffuse aurora.

Diffuse electron precipitation is determined by the plasmashet distribution of electrons that are deposited into the ionosphere-thermosphere (Ni et al., 2016). Global magnetohydrodynamic (MHD) models of the magnetosphere traditionally implement auroral precipitation via empirical parameterization of MHD variables of plasma density, temperature, and field-aligned current (FAC) (e.g., Fedder et al., 1995; Raeder et al., 2001). However, diffuse precipitation obtained from an MHD parameterization intrinsically lacks some key features of the source electron population that are caused by their energy-dependent drifts, not included in MHD models, e.g., dawn-dusk asymmetry. In order to obtain a diffuse precipitation distribution consistent with the statistics of Newell et al. (2009), Zhang et al. (2015) introduced an empirical diffuse precipitation mask in a global MHD magnetospheric model to represent the eastward drift of electrons, which lacked self-consistency and dynamic variability. Ring current models have been recently used to derive diffuse electron precipitation based on kinetic physics (e.g. Fok et al., 2014; Chen et al., 2015; Yu et al., 2016). For example, Yu et al. (2016) calculated the pitch angle diffusion coefficients associated with whistler mode chorus and hiss waves, which resulted in diffuse electron precipitation in better agreement with satellite measurements than MHD-based results.

This study focuses on the influence of diffuse electron precipitation on MIT coupling with a particular emphasis on mesoscale SAPS structure. In order to systematically understand its role, diffuse precipitation is implemented in a fully coupled geospace model by making use of electron distribution determined by tracking their energy-dependent drifts. In the newly developed Multiscale Atmosphere-Geospace Environment (MAGE) model, diffuse electron precipitation is derived from the electron distribution in a ring current model, which solves for the bounce-averaged drifts of particles. The diffuse precipitation together with MHD-based mono-energetic electron precipitation are input to a general circulation ionosphere-thermosphere (IT) model to characterize the IT response and feedback. SAPS in the 17 March 2013 geomagnetic storm event are revisited with the MAGE model. The drift physics-informed precipitation and the fully coupled geospace model of MAGE, as will be elaborated in this paper, represent an important advance in characterizing auroral precipitation in geospace models and show significant improvements in resolving SAPS at mesoscales. Using the fully coupled first-principles MAGE model, we illustrate the formation of SAPS as a manifestation of the collective dynamic behavior of the coupled MIT system.

**Figure 1.** (a) Diagram of the MAGE model. (b-f) Solar wind/IMF and SYMH index for 17 March 2013 from CDAWeb OMNI data product.

## 2 Model Description

MAGE is a coupled model for simulating the geospace system, developed at the NASA DRIVE Science Center for Geospace Storms. This study is based on the current iteration of the MAGE model, whose diagram is illustrated in Figure 1a. MAGE consists of the Grid Agnostic MHD with Extended Research Applications (GAMERA) global MHD model of the magnetosphere (Zhang et al., 2019a; Sorathia et al., 2020), the Rice Convection Model (RCM) model of the ring current (Toffoletto et al., 2003), Thermosphere-Ionosphere Electrodynamics General Circulation Model (TIEGCM) of the upper atmosphere (Richmond et al., 1992), and RE-developed Magnetosphere-Ionosphere Coupler/Solver (REMIX) (Merkin & Lyon, 2010). GAMERA carries on the legacy of its predecessor, the Lyon-Fedder-Mobarry (LFM) model (Lyon et al., 2004) as described by (Sorathia et al., 2020). The coupling between the different MAGE components is conceptually similar to the previous coupled geospace model developed by the same group (e.g., Lin et

131 al., 2019), but the software implementation is entirely new and will be described in more  
 132 detail elsewhere.

133 MAGE implements an electron precipitation model that takes into account the distinct  
 134 physical driving mechanisms for the diffuse and mono-energetic electron precipi-  
 135 tation. As illustrated in Figure 1a, mono-energetic electron precipitation is derived from  
 136 MHD density, temperature, and FAC on the inner boundary of GAMERA (at two Earth  
 137 radii) based on the formulation of Zhang et al. (2015). Only the precipitation that un-  
 138 dergoes field-aligned electrostatic potential drop is adopted as the mono-energetic elec-  
 139 tron precipitation in MAGE. Precipitation anywhere else is treated as diffuse electron  
 140 precipitation and uses the results derived from RCM, which solves bounce-averaged drift  
 141 motion of ring current electrons and ions. The diffuse precipitation is calculated by in-  
 142 tegrating the electron distribution function in RCM and assuming that the precipitation  
 143 loss rate is one third of that derived from strong pitch angle scattering (Wolf, 1983; Schu-  
 144 maker et al., 1989; Bao, 2019). These two types of precipitating electrons (mono-energetic  
 145 and diffuse) are combined in REMIX and passed to TIEGCM to calculate ionospheric  
 146 ionization rate and electron density, the magnitude and distribution of ionospheric con-  
 147 ductivity, and height-integrated conductance. RCM has also been improved in MAGE  
 148 to include a zero-energy channel to model the cold plasmaspheric mass. The dynamic  
 149 plasmasphere is initialized with the Gallagher empirical model (Gallagher et al., 1988)  
 150 and then evolved self-consistently using the electrostatic potential from REMIX with added  
 151 corotation. This improvement to RCM will be described in detail elsewhere.

152 In this study, GAMERA uses  $96 \times 96 \times 128$  grid cells in the radial, meridional,  
 153 and azimuthal directions, respectively, where the spherical symmetry axis of the grid is  
 154 pointing from Earth to Sun. RCM uses  $200 \times 100 \times 90$  grid cells in the latitudinal, lon-  
 155 gitudinal (in Solar Magnetic, SM, coordinates), and energy dimensions, respectively. In  
 156 the energy dimension, 27 energy channels are for electrons, 62 energy channels for pro-  
 157 tons, and 1 zero-energy channel for the cold plasmasphere. REMIX grid uses  $45 \times 360$   
 158 grid cells in the latitudinal and longitudinal directions (in SM), respectively. Its reso-  
 159 lution is  $1^\circ$  in both dimensions and the low latitude boundary is at  $45^\circ$  magnetic lati-  
 160 tude (MLAT). TIEGCM uses  $288 \times 144 \times 57$  cells in longitudinal, latitudinal, and alti-  
 161 tudinal directions (in geographic coordinate system), respectively. It has a uniform hor-  
 162 izontal resolution of  $1.25^\circ$  and a vertical pressure grid of 0.25 scale height. GAMERA  
 163 and TIEGCM both adopt a ring-average technique to treat the spherical axis of their  
 164 respective grids (Zhang et al., 2019b; Dang et al., 2020). GAMERA and RCM exchange  
 165 information every 15 s, GAMERA and REMIX every 5 s, and REMIX and TIEGCM  
 166 every 5 s.

### 167 3 Data-Model Comparison

168 MAGE is used to simulate the well-known St. Patrick’s Day geomagnetic storm  
 169 on 17 March 2013. The solar wind and IMF conditions to drive the simulation are shown  
 170 in Figure 1b-1e, which are obtained from the CDAWeb OMNI data product with 1 minute  
 171 resolution. OMNI data gaps are filled with linear interpolation. The geomagnetic storm  
 172 was triggered by a coronal mass ejection (CME) which arrived at Earth at 05:55 UT.  
 173 The solar wind density increased to  $10 \text{ cm}^{-3}$  and solar wind  $V_X$  to 700 km/s across the  
 174 CME shock. During the storm the IMF  $B_Z$  component was mostly southward with oc-  
 175 casional northward turnings, the strongest  $B_Z$  was nearly -20 nT. The SYMH index dropped  
 176 to below -100 nT in the main phase.

177 SAPS structures are analyzed by comparing the simulation results with observa-  
 178 tional data. Figure 2 shows DMSP F18 measurements during three duskside auroral cross-  
 179 ings in black curves. MAGE simulation results are sampled along the F18 trajectory and  
 180 shown in red curves. From top to bottom the rows show the integrated electron precipi-  
 181 tation energy flux (EnFlux), horizontal ion drifts along the cross track direction of DMSP

182 F18 ( $V_{\text{HD}}$ ), FAC density (positive downward), and Pedersen conductance ( $\Sigma_{\text{P}}$ ). DMSP  
 183 EnFlux and  $V_{\text{HD}}$  are smoothed with a 15 s moving mean of the original 1 s resolution  
 184 data. The DMSP FACs are smoothed with a 60 s moving mean of the 1 s resolution re-  
 185 sults provided by Xiong et al. (2020). MAGE results are output by REMIX every 15 s.

186 The electron auroral equatorward boundary is defined where EnFlux drops to 10%  
 187 of the peak value in each crossing. For example, during the crossing between 08:28 and  
 188 08:38 UT (Figure 2a) MAGE simulated electron auroral equatorward boundary was at  
 189  $\sim 62^\circ$  MLAT, as indicated by the vertical blue dashed line in the first column. To the  
 190 left of the blue line is the subauroral region shaded in magenta. The DMSP-measured  
 191 electron auroral equatorward boundary was located at  $\sim 65^\circ$  MLAT by referring to the  
 192 black curve in Figure 2a. Figure 2b compares the simulated and measured  $V_{\text{HD}}$  during  
 193 the 08:28-08:38 UT auroral crossing. The subauroral flow channel occurs below  $62^\circ$  MLAT  
 194 in the MAGE results (note the secondary bump in the red trace), which is identified as  
 195 SAPS. DMSP measured  $V_{\text{HD}}$  also shows a SAPS channel below  $\sim 63^\circ$  MLAT. During  
 196 this auroral crossing, downward FACs are seen between  $\sim 55^\circ$  and  $63\text{--}64^\circ$  MLAT (Fig-  
 197 ure 2c). Here downward FACs are defined as positive in both hemispheres, shaded in green.  
 198 Note DMSP measured FACs almost overlap with the MAGE FACs. The magenta and  
 199 green shaded regions in Figure 2b reveal that the SAPS channel is mostly sandwiched  
 200 by the equatorward boundaries of electron aurora and downward FAC. Figure 2d shows  
 201 the MAGE simulated  $\Sigma_{\text{P}}$  which drops dramatically equatorward of the electron precip-  
 202 itation boundary.

203 The right two columns of Figure 2 show MAGE-DMSP comparison in the same for-  
 204 mat for two other auroral crossings in the duskside southern hemisphere during 11:18-  
 205 11:28 UT and 13:00-13:10 UT, respectively. The simulated SAPS locations are very close  
 206 to those from DMSP measurements. Although the peak magnitudes are sometimes dif-  
 207 ferent by a few hundred m/s, the MAGE-simulated latitudinal structures of ion drifts  
 208 in these three examples are similar to those in the DMSP data and reveal the SAPS chan-  
 209 nel unambiguously. A comparison of FAC with Active Magnetosphere and Planetary Elec-  
 210 trodynamics Response Experiment (AMPERE) measurements also validates the spatial  
 211 distribution of large-scale FAC from the simulation results, which are shown in the Sup-  
 212 porting Information (Figure S1).

213 The sampled EnFlux from MAGE is mostly diffuse precipitation during the cross-  
 214 ing between 08:28 UT and 08:38 UT although DMSP energy spectrum shows mono-energetic  
 215 precipitation features for that single peak collocated with upward FAC. Two EnFlux peaks  
 216 were detected by DMSP and simulated by MAGE during the crossing between 11:18 UT  
 217 and 11:28 UT. The equatorward one is diffuse precipitation and the poleward one was  
 218 mono-energetic precipitation. During the auroral crossing from 13:00 UT to 13:10 UT  
 219 DMSP F18 detected three EnFlux peaks, the most equatorward one was diffuse precip-  
 220 itation while the poleward two were mono-energetic precipitation associated with up-  
 221 ward FAC structures. Additional comparison of EnFlux and  $V_{\text{HD}}$  between MAGE sim-  
 222 ulations and multiple DMSP satellite measurements is provided in the Supporting In-  
 223 formation (Movie S1).

224 In order to better understand the role of diffuse precipitation in generating and shap-  
 225 ing SAPS, a controlled experiment was conducted by turning off diffuse precipitation in  
 226 the MAGE model and compared with the baseline run including diffuse precipitation shown  
 227 in Figure 2. Figure 3 shows the simulation results at 11:10 UT from the baseline run in  
 228 the top row and from the run with diffuse precipitation off in the bottom row. The first  
 229 three columns from left to right show EnFlux, FAC, and westward ion drifts (WID) in  
 230 the northern hemisphere ionosphere output by REMIX, respectively. The magenta curves  
 231 show EnFlux contour level of  $1.0 \text{ mW/m}^2$  and are used to indicate the auroral bound-  
 232 aries. The green curves show FAC contour level of  $0.2 \text{ }\mu\text{A/m}^2$  and indicate the down-  
 233 ward FAC boundaries. The two boundaries are over-plotted on top of WID in Figures  
 234 3c and 3g.

235 Figures 3d and 3h show the latitudinal distributions of EnFlux, FAC, and WID with  
 236 magenta, green, and blue curves, respectively, which are sampled across MLAT at 20 hours  
 237 magnetic local time (MLT). Figure 3d shows a mono-energetic electron precipitation peak  
 238 at around 70° MLAT and a diffuse precipitation peak at around 62° MLAT in the base-  
 239 line run. Diffuse precipitation is located in the high latitude part of the downward Re-  
 240 gion 2 (R2) FAC. A SAPS channel is clearly visible between  $\sim 53^\circ$  and  $58^\circ$  MLAT with  
 241 a peak velocity of  $\sim 1.3$  km/s at  $\sim 56^\circ$  MLAT. This SAPS channel is equatorward of  
 242 the diffuse precipitation and in the downward R2 FAC region. In the run with diffuse  
 243 precipitation turned off (Figure 3h), there is only one auroral band consisting of mono-  
 244 energetic electron precipitation and collocated with the upward (negative) FAC. The sub-  
 245 auroral convection is nearly 20° broad latitudinally from  $\sim 53^\circ$  to  $\sim 73^\circ$  MLAT.

246 The two-dimensional distributions of ionospheric convection and their relative lo-  
 247 cations to EnFlux and FAC in these two model runs are illustrated in Figure 3a-3c, 3e-  
 248 3g. Figure 3a shows that in the baseline run, the electron auroral equatorward bound-  
 249 ary is located at around 64° MLAT from 16 to 19 MLT and at around 60° MLAT from  
 250 19 MLT through the dawnside to 12 MLT. With diffuse precipitation off, the electron  
 251 auroral equatorward boundary is at around 70° MLAT, above which mono-energetic elec-  
 252 tron precipitation is concentrated in the duskside upward Region 1 (R1) FAC (Figure  
 253 3e). It is the diffuse precipitation that moves the electron auroral equatorward bound-  
 254 ary to a lower latitude in the MLT sector from post-dusk to dawn. Figure 3c shows SAPS  
 255 as a separate enhanced westward flow channel inside the R2 FAC in the dusk sector. In  
 256 the run with diffuse precipitation off, however, the auroral equatorward boundary is at  
 257 a much higher latitude and subauroral plasma convection spans more than 10° in lat-  
 258 itude and exhibits no mesoscale SAPS structure evident in Figure 3g.

259 SAPS are generated in the subauroral region as a result of current closure. Equa-  
 260 torward of the auroral precipitation, the ionospheric conductance drops dramatically due  
 261 to lack of precipitating particles to ionize the neutral atmosphere, especially after sun-  
 262 set when solar radiation vanishes. Such latitudinal variations of  $\Sigma_P$  are verified in the  
 263 MAGE simulation and shown in Figures 2d, 2h, and 2l. However, since the equatorward  
 264 boundary of downward FAC is at a lower latitude than the electron precipitation low lat-  
 265 itude boundary, there are still substantial R2 FACs that need to be closed in the gap be-  
 266 tween the two low latitude boundaries (Figure 3c). Due to Ohm's law, the relatively low  
 267 conductance between the two boundaries results in an enhanced poleward electric field  
 268 to drive the Pedersen currents to flow poleward. That strong electric field then produces  
 269 enhanced westward ion drifts (SAPS) in the subauroral region.

270 The gap between the equatorward boundaries of FAC and EnFlux can be traced  
 271 back to the magnetosphere. Figure 4 illustrates the SAPS driving mechanism from the  
 272 perspective of the coupled magnetosphere-ionosphere. The ionospheric zonal ion drifts  
 273 are shown on the white hemisphere with a red-blue colormap, where red indicates west-  
 274 ward drifts. The inset presents an amplified view of the SAPS channel in the dusk sec-  
 275 tor, which is sandwiched by the low latitude boundaries of electron precipitation (ma-  
 276 genta) and downward FAC (green). The boundaries are mapped along the geomagnetic  
 277 field lines to the magnetospheric equatorial plane, where the plasma density is represented  
 278 with a purple-yellow colormap. The semi-transparent surfaces show the near-equatorial  
 279 part of the geomagnetic field lines connecting the EnFlux/FAC boundaries in the mag-  
 280 netosphere and ionosphere. The gap between the ionospheric low latitude boundaries of  
 281 EnFlux and downward FAC is projected to the region between their inner boundaries  
 282 in the equatorial plane, as pointed out by the blue arrows. In the magnetospheric plas-  
 283 masheet, downward FAC is primarily determined by the ion pressure distribution while  
 284 the electron precipitation is uniquely populated by the electron distribution. Since plas-  
 285 masheet ions typically penetrate deeper than the electrons, the inner edge of the ion dis-  
 286 tribution is more inward than the electrons (e.g. Califf et al., 2016). The downward FAC

287 inner boundary is therefore more inward than that of the electron precipitation, which  
288 forms the gap region where SAPS are generated.

## 289 4 Conclusion and Discussion

290 In this study we explored the role of diffuse electron precipitation in the formation  
291 of SAPS using the state-of-the-art coupled geospace model, MAGE. Diffuse precipita-  
292 tion is derived from the electron distribution solved for by the RCM component of MAGE.  
293 The diffuse precipitation, informed by the ring current model including energy-dependent  
294 drifts, is an important advance in characterizing the major component of auroral precipi-  
295 tation in geospace models compared to the traditional approach of MHD-based pa-  
296 rameterizations. The particle distribution-based diffuse precipitation and MHD-based  
297 mono-energetic electron precipitation are combined as inputs for an ionosphere-thermosphere  
298 model to calculate ionospheric conductance, which is done here for the first time in a fully  
299 coupled geospace model. MAGE simulation results of the 17 March 2013 geomagnetic  
300 storm captured unambiguous SAPS structures that are in a good agreement with DMSP  
301 F18 measurements. Controlled numerical experiments further demonstrate the critical  
302 role of diffuse precipitation in the formation of SAPS, i.e. SAPS manifest themselves as  
303 a separate subauroral flow channel when diffuse precipitation is included in the simu-  
304 lation whereas they merge with the primary auroral convection when the diffuse precipi-  
305 tation is turned off. The driving mechanism of SAPS is illustrated from the perspec-  
306 tive of coupled magnetosphere-ionosphere. Since the ring current protons penetrate deeper  
307 than the electrons in the duskside inner magnetosphere, the inner edge of proton ring  
308 current is closer to the Earth than the inner edge of the electron plasmashet. When mapped  
309 to the duskside ionosphere, the equatorward boundary of downward FAC is below that  
310 of the electron precipitation, leaving R2 FAC requiring closure in the low conductance  
311 subauroral region. An enhanced poleward electric field is generated to drive the high speed  
312 westward plasma flow of SAPS (Anderson et al., 2001).

313 This investigation on how the diffuse electron precipitation impacts the formation  
314 of SAPS is enabled by the new modeling capabilities developed in MAGE. Diffuse precipi-  
315 tation is directly derived from the electron distribution function in the RCM which  
316 tracks the energy-dependent particle drifts. The resultant diffuse precipitation shows a  
317 natural dawnward rotation due to the eastward drift of electrons in the inner magneto-  
318 sphere (Figure 3a), which is intrinsically absent in the MHD description. An even more  
319 sophisticated diffuse precipitation has been recently derived from a kinetic ring current  
320 model by taking into account wave-particle interactions (Yu et al., 2016). In this paper,  
321 we take a further step in improving the physical description of diffuse precipitation in  
322 the MIT system by coupling to a physics-based model of the ionosphere-thermosphere,  
323 which computes the ionospheric conductivity self-consistently, given the precipitating elec-  
324 tron fluxes. This, in turn, enabled a comprehensive investigation of SAPS, which requires  
325 all of the ingredients included in our model simultaneously: a ring current model, which  
326 correctly tracks the electron and ion drifts and the earthward boundaries of their mag-  
327 netospheric distributions, in combination with a self-consistent ionosphere-magnetosphere  
328 model.

329 Our results suggest a number of further improvements to the MAGE model. The  
330 comparison with DMSP measurements (Figure 2) indicates that the model resolution  
331 is still not sufficient to capture the observed variability of the ionospheric precipitation,  
332 FACs and convection. While the individual MAGE components have been run at a sig-  
333 nificantly higher resolution separately (e.g., Sorathia et al., 2020; Dang et al., 2020), such  
334 a high-resolution coupled MAGE simulation is currently in development. Furthermore,  
335 SAPS are missed toward the dayside in the model when comparing with DMSP F16 and  
336 F17, which crossed the duskside auroral oval closer to noon, as shown in the Support-  
337 ing Information. This can be attributed to the underestimated precipitation in the post-  
338 noon sector, implying the uniform electron loss rate in RCM may be oversimplified. Fi-

nally, currently only mono-energetic electron precipitation and diffuse precipitation are implemented in the MAGE precipitation model, which is justified as a first step by their statistically dominant contribution to the total precipitation energy and number flux (Newell et al., 2009). However, other types of precipitation such as ion precipitation can also play a role in the generation of localized structures and dynamics, especially in the subauroral SAPS region (e.g. Yuan et al., 2016). These particle and energy inputs will be included in the future iterations of the MAGE model.

## Acknowledgments

Dong Lin is supported by the Advanced Study Program (ASP) Postdoctoral Fellowship of National Center for Atmospheric Research (NCAR). NCAR is sponsored by National Science Foundation (NSF). This work is supported by NASA GCR grant 80NSSC17K0013, LWS grants 80NSSC20K0356 and 80NSSC19K0080, the DRIVE Science Center for Geospace Storms (CGS) under grant 80NSSC20K0601, NASA O2R grant 80NSSC19K0241, and NCAR System for Integrated Modeling of the Atmosphere (SIMA) reinvestment fund. We would like to acknowledge high-performance computing support from Cheyenne (doi:10.5065/D6RX99HX) provided by NCAR’s Computational and Information Systems Laboratory. Dong Lin is thankful to Dr. Simon Wing and Dr. Thomas Sotirelis for the discussions on DMSP data, to Dr. Chao Xiong for the DMSP FAC results, and to Dr. Gang Lu for the internal review. The OMNI data are available at <https://cdaweb.gsfc.nasa.gov/index.html/>. The DMSP SSJ and SSIES data are obtained from <https://satdat.ngdc.noaa.gov/dmsp/data/> and FAC data from <ftp://magftp.gfz-potsdam.de/DMSP/FAC/>. The AMPERE data are obtained from <http://ampere.jhuapl.edu/>. The simulation data are archived in <https://doi.org/10.5065/xaz4-cc27>.

## References

- Anderson, P., Carpenter, D., Tsuruda, K., Mukai, T., & Rich, F. (2001). Multisatellite observations of rapid subauroral ion drifts (SAID). *Journal of Geophysical Research: Space Physics*, *106*(A12), 29585–29599. doi: 10.1029/2001JA000128
- Bao, S. (2019). *Large-scale coupled models of the inner magnetosphere* (Doctoral dissertation, Rice University). doi: <https://hdl.handle.net/1911/107801>
- Califf, S., Li, X., Wolf, R., Zhao, H., Jaynes, A., Wilder, F., . . . Redmon, R. (2016). Large-amplitude electric fields in the inner magnetosphere: Van Allen Probes observations of subauroral polarization streams. *Journal of Geophysical Research: Space Physics*, *121*(6), 5294–5306. doi: 10.1002/2015JA022252
- Chen, M. W., Lemon, C. L., Orlova, K., Shprits, Y., Hecht, J., & Walterscheid, R. (2015). Comparison of simulated and observed trapped and precipitating electron fluxes during a magnetic storm. *Geophysical Research Letters*, *42*(20), 8302–8311. doi: 10.1002/2015GL065737
- Dang, T., Zhang, B., Lei, J., Wang, W., Burns, A., Liu, H.-l., . . . Sorathia, K. A. (2020). Development of high-resolution thermosphere-ionosphere electrodynamics general circulation model (TIE-GCM) using ring average technique. *Geoscientific Model Development Discussions*, 1–30. doi: 10.5194/gmd-2020-243
- Ebihara, Y., Nishitani, N., Kikuchi, T., Ogawa, T., Hosokawa, K., Fok, M.-C., & Thomsen, M. (2009). Dynamical property of storm time subauroral rapid flows as a manifestation of complex structures of the plasma pressure in the inner magnetosphere. *Journal of Geophysical Research: Space Physics*, *114*(A1). doi: 10.1029/2008JA013614
- Fedder, J. A., Slinker, S. P., Lyon, J. G., & Elphinstone, R. (1995). Global numerical simulation of the growth phase and the expansion onset for a substorm observed by Viking. *Journal of Geophysical Research: Space Physics*, *100*(A10),

- 19083–19093. doi: 10.1029/95JA01524
- 390  
391 Ferdousi, B., Nishimura, Y., Maruyama, N., & Lyons, L. R. (2019). Subauroral  
392 neutral wind driving and its feedback to SAPS during the 17 March 2013 ge-  
393 omagnetic storm. *Journal of Geophysical Research: Space Physics*, *124*(3),  
394 2323–2337. doi: 10.1029/2018JA026193
- 395 Fok, M.-C., Buzulukova, N., Chen, S.-H., Glocer, A., Nagai, T., Valek, P., & Perez,  
396 J. (2014). The comprehensive inner magnetosphere-ionosphere model.  
397 *Journal of Geophysical Research: Space Physics*, *119*(9), 7522–7540. doi:  
398 10.1002/2014JA020239
- 399 Foster, J., Holt, J. M., Musgrove, R., & Evans, D. (1986). Ionospheric convection as-  
400 sociated with discrete levels of particle precipitation. *Geophysical Research Let-*  
401 *ters*, *13*(7), 656–659. doi: 10.1029/GL013i007p00656
- 402 Foster, J., & Vo, H. (2002). Average characteristics and activity dependence of  
403 the subauroral polarization stream. *Journal of Geophysical Research: Space*  
404 *Physics*, *107*(A12), SIA–16. doi: 10.1029/2002JA009409
- 405 Gallagher, D., Craven, P., & Comfort, R. (1988). An empirical model of the Earth’s  
406 plasmasphere. *Advances in space research*, *8*(8), 15–24. doi: 10.1016/0273-  
407 -1177(88)90258-X
- 408 Guo, J.-P., Deng, Y., Zhang, D.-H., Lu, Y., Sheng, C., & Zhang, S.-R. (2018). The  
409 effect of subauroral polarization streams on ionosphere and thermosphere dur-  
410 ing the 2015 St. Patrick’s Day storm: Global ionosphere-thermosphere model  
411 simulations. *Journal of Geophysical Research: Space Physics*, *123*(3), 2241–  
412 2256. doi: 10.1002/2017JA024781
- 413 Hardy, D. A., Gussenhoven, M., Raistrick, R., & McNeil, W. (1987). Statistical and  
414 functional representations of the pattern of auroral energy flux, number flux,  
415 and conductivity. *Journal of Geophysical Research: Space Physics*, *92*(A11),  
416 12275–12294. doi: 10.1029/JA092iA11p12275
- 417 He, F., Zhang, X.-X., Wang, W., & Wan, W. (2017). Different evolution pat-  
418 terns of subauroral polarization streams (SAPS) during intense storms  
419 and quiet time substorms. *Geophysical Research Letters*, *44*(21). doi:  
420 10.1002/2017GL075449
- 421 Hill, T., Dessler, A., & Wolf, R. (1976). Mercury and Mars: The role of ionospheric  
422 conductivity in the acceleration of magnetospheric particles. *Geophysical Re-*  
423 *search Letters*, *3*(8), 429–432. doi: 10.1029/GL003i008p00429
- 424 Huang, C.-S. (2020). Westward plasma drifts in the nighttime equatorial ionosphere  
425 during severe magnetic storms: A new type of penetration electric fields caused  
426 by subauroral polarization stream. *Journal of Geophysical Research: Space*  
427 *Physics*, *125*(10), e2020JA028300. doi: 10.1029/2020JA028300
- 428 Jensen, J. B., Raeder, J., Maynard, K., & Cramer, W. D. (2017). Particle precip-  
429 itation effects on convection and the magnetic reconnection rate in Earth’s  
430 magnetosphere. *Journal of Geophysical Research: Space Physics*, *122*(11),  
431 11–413. doi: 10.1002/2017JA024030
- 432 Kunduri, B., Baker, J., Ruohoniemi, J., Thomas, E., Shepherd, S., & Sterne, K.  
433 (2017). Statistical characterization of the large-scale structure of the subau-  
434 roral polarization stream. *Journal of Geophysical Research: Space Physics*,  
435 *122*(6), 6035–6048. doi: 10.1002/2017JA024131
- 436 Lin, D., Wang, W., Scales, W. A., Pham, K., Liu, J., Zhang, B., . . . Maimaiti, M.  
437 (2019). SAPS in the 17 March 2013 storm event: Initial results from the cou-  
438 pled magnetosphere-ionosphere-thermosphere model. *Journal of Geophysical*  
439 *Research: Space Physics*, *124*(7), 6212–6225. doi: 10.1029/2019JA026698
- 440 Lyon, J., Fedder, J., & Mobarry, C. (2004). The Lyon–Fedder–Mobarry  
441 (LFM) global MHD magnetospheric simulation code. *Journal of At-*  
442 *mospheric and Solar-Terrestrial Physics*, *66*(15–16), 1333–1350. doi:  
443 10.1016/j.jastp.2004.03.020
- 444 McGranaghan, R., Knipp, D. J., Matsuo, T., Godinez, H., Redmon, R. J., Solomon,

- 445 S. C., & Morley, S. K. (2015). Modes of high-latitude auroral conductance  
446 variability derived from DMSP energetic electron precipitation observations:  
447 Empirical orthogonal function analysis. *Journal of Geophysical Research:*  
448 *Space Physics*, *120*(12), 11–013. doi: 10.1002/2015JA021828
- 449 Merkin, V., & Lyon, J. (2010). Effects of the low-latitude ionospheric boundary con-  
450 dition on the global magnetosphere. *Journal of Geophysical Research: Space*  
451 *Physics*, *115*(A10). doi: 10.1029/2010JA015461
- 452 Merkin, V., Papadopoulos, K., Milikh, G., Sharma, A., Shao, X., Lyon, J., &  
453 Goodrich, C. (2003). Effects of the solar wind electric field and ionospheric  
454 conductance on the cross polar cap potential: Results of global MHD model-  
455 ing. *Geophysical Research Letters*, *30*(23). doi: 10.1029/2003GL017903
- 456 Merkin, V., Sharma, A., Papadopoulos, K., Milikh, G., Lyon, J., & Goodrich, C.  
457 (2005). Global MHD simulations of the strongly driven magnetosphere: Mod-  
458 eling of the transpolar potential saturation. *Journal of Geophysical Research:*  
459 *Space Physics*, *110*(A9). doi: 10.1029/2004JA010993
- 460 Newell, P., Sotirelis, T., & Wing, S. (2009). Diffuse, monoenergetic, and broadband  
461 aurora: The global precipitation budget. *Journal of Geophysical Research:*  
462 *Space Physics*, *114*(A9). doi: 10.1029/2009JA014326
- 463 Ni, B., Thorne, R. M., Zhang, X., Bortnik, J., Pu, Z., Xie, L., . . . others (2016).  
464 Origins of the Earths diffuse auroral precipitation. *Space Science Reviews*,  
465 *200*(1-4), 205–259. doi: 10.1007/s11214-016-0234-7
- 466 Raeder, J., Cramer, W. D., Jensen, J., Fuller-Rowell, T., Maruyama, N., Toffo-  
467 letto, F., & Vo, H. (2016). Sub-auroral polarization streams: A com-  
468 plex interaction between the magnetosphere, ionosphere, and thermo-  
469 sphere. In *Journal of physics: Conference series* (Vol. 767, p. 012021). doi:  
470 10.1088/1742-6596/767/1/012021
- 471 Raeder, J., McPherron, R., Frank, L., Kokubun, S., Lu, G., Mukai, T., . . . Slavin,  
472 J. (2001). Global simulation of the Geospace Environment Modeling substorm  
473 challenge event. *Journal of Geophysical Research: Space Physics*, *106*(A1),  
474 381–395. doi: 10.1029/2000JA000605
- 475 Richmond, A., Ridley, E., & Roble, R. (1992). A thermosphere/ionosphere general  
476 circulation model with coupled electrodynamics. *Geophysical Research Letters*,  
477 *19*(6), 601–604. doi: 10.1029/92GL00401
- 478 Schumaker, T. L., Gussenhoven, M. S., Hardy, D. A., & Carovillano, R. L. (1989).  
479 The relationship between diffuse auroral and plasma sheet electron distribu-  
480 tions near local midnight. *Journal of Geophysical Research: Space Physics*,  
481 *94*(A8), 10061–10078. doi: 10.1029/JA094iA08p10061
- 482 Sorathia, K., Merkin, V., Panov, E., Zhang, B., Lyon, J., Garretson, J., . . . Wilt-  
483 berger, M. (2020). Ballooning-interchange instability in the near-Earth plasma  
484 sheet and auroral beads: Global magnetospheric modeling at the limit of the  
485 MHD approximation. *Geophysical research letters*, *47*(14), e2020GL088227.  
486 doi: 10.1029/2020GL088227
- 487 Southwood, D., & Wolf, R. (1978). An assessment of the role of precipitation in  
488 magnetospheric convection. *Journal of Geophysical Research: Space Physics*,  
489 *83*(A11), 5227–5232. doi: 10.1029/JA083iA11p05227
- 490 Toffoletto, F., Sazykin, S., Spiro, R., & Wolf, R. (2003). Inner magnetospheric mod-  
491 eling with the Rice Convection Model. *Space Science Reviews*, *107*(1-2), 175–  
492 196. doi: 10.1023/A:1025532008047
- 493 Wang, W., Talaat, E. R., Burns, A. G., Emery, B., Hsieh, S.-y., Lei, J., & Xu, J.  
494 (2012). Thermosphere and ionosphere response to subauroral polarization  
495 streams (SAPS): Model simulations. *Journal of Geophysical Research: Space*  
496 *Physics*, *117*(A7). doi: 10.1029/2012JA017656
- 497 Wolf, R. (1983). The quasi-static (slow-flow) region of the magnetosphere. In *Solar-*  
498 *terrestrial physics* (pp. 303–368). Springer. doi: 10.1007/978-94-009-7194-3\_14
- 499 Xiong, C., Stolle, C., Alken, P., & Rauberg, J. (2020). Relationship between

- 500 large-scale ionospheric field-aligned currents and electron/ion precipita-  
501 tions: DMSP observations. *Earth, Planets and Space*, 72(1), 1–22. doi:  
502 10.1186/s40623-020-01286-z
- 503 Yu, Y., Jordanova, V., Zou, S., Heelis, R., Ruohoniemi, M., & Wygant, J. (2015).  
504 Modeling subauroral polarization streams during the 17 March 2013 storm.  
505 *Journal of Geophysical Research: Space Physics*, 120(3), 1738–1750. doi:  
506 10.1002/2014JA020371
- 507 Yu, Y., Jordanova, V. K., Ridley, A. J., Albert, J. M., Horne, R. B., & Jeffery, C. A.  
508 (2016). A new ionospheric electron precipitation module coupled with RAM-  
509 SCB within the geospace general circulation model. *Journal of Geophysical*  
510 *Research: Space Physics*, 121(9), 8554–8575. doi: 10.1002/2016JA022585
- 511 Yuan, Z., Qiao, Z., Li, H., Huang, S., Wang, D., Yu, X., & Yu, T. (2017). Subau-  
512 roral polarization stream on the outer boundary of the ring current during an  
513 energetic ion injection event. *Journal of Geophysical Research: Space Physics*,  
514 122(4), 4837–4845. doi: 10.1002/2016JA023570
- 515 Yuan, Z., Xiong, Y., Qiao, Z., Li, H., Huang, S., Wang, D., . . . Wang, J. (2016).  
516 A subauroral polarization stream driven by field-aligned currents associ-  
517 ated with precipitating energetic ions caused by EMIC waves: A case study.  
518 *Journal of Geophysical Research: Space Physics*, 121(2), 1696–1705. doi:  
519 10.1002/2015JA021804
- 520 Zhang, B., Lotko, W., Brambles, O., Wiltberger, M., & Lyon, J. (2015). Electron  
521 precipitation models in global magnetosphere simulations. *Journal of Geophys-*  
522 *ical Research: Space Physics*, 120(2), 1035–1056. doi: 10.1002/2014JA020615
- 523 Zhang, B., Sorathia, K. A., Lyon, J. G., Merkin, V. G., Garretson, J. S., & Wilt-  
524 berger, M. (2019a). Gamera: A three-dimensional finite-volume MHD solver  
525 for non-orthogonal curvilinear geometries. *The Astrophysical Journal Supple-*  
526 *ment Series*, 244(1), 20. doi: 10.3847/1538-4365/ab3a4c
- 527 Zhang, B., Sorathia, K. A., Lyon, J. G., Merkin, V. G., & Wiltberger, M. (2019b).  
528 Conservative averaging-reconstruction techniques (Ring Average) for 3-D  
529 finite-volume MHD solvers with axis singularity. *Journal of Computational*  
530 *Physics*, 376, 276–294. doi: 10.1016/j.jcp.2018.08.020
- 531 Zheng, Y., Brandt, P. C., Lui, A. T., & Fok, M.-C. (2008). On ionospheric  
532 trough conductance and subauroral polarization streams: Simulation re-  
533 sults. *Journal of Geophysical Research: Space Physics*, 113(A4). doi:  
534 10.1029/2007JA012532

**Figure 2.** Comparison of DMSP F18 measurements (black) and MAGE simulation results (red) during three duskside auroral crossings. From top to bottom are integrated electron precipitation energy flux (EnFlux), cross track ion drift velocity ( $V_{HD}$ ), FAC density, and Pedersen conductance ( $\Sigma_P$ ). The blue vertical dashed lines indicate the equatorward auroral boundaries in MAGE results, defined as where EnFlux is 0.1 of the peak value in the aurora. The subauroral regions are shaded in magenta. Downward FAC (positive) regions are shaded in green.

**Figure 3.** Comparison between with (top row) and without (bottom row) diffuse precipitation in MAGE simulations of SAPS. The left three columns are EnFlux, FAC density, and westward ion drifts (WID) in the northern hemisphere ionosphere from REMIX outputs. The magenta curves are EnFlux contour level of  $1.0 \text{ mW/m}^2$ . The green curves are FAC contour level of  $0.2 \text{ } \mu\text{A/m}^2$ . WID has the corotation velocity added. The fourth column shows the latitudinal distributions of EnFlux (magenta), FAC (green), and WID (blue) sampled at 20 hours MLT.

**Figure 4.** SAPS viewed from the ionosphere and magnetosphere. The white hemisphere near the axis origin on top of the orange square represents the northern hemisphere ionosphere. The red-blue colors represent westward and eastward ion drifts, respectively. The high latitude part of the hemisphere is amplified in the inset plot for better visibility. The low latitude one of the two red belts represents SAPS. The purple-yellow colors represent the plasma density distribution in the magnetospheric equatorial plane. The magenta and green curves represent the electron precipitation boundary and duskside downward FAC boundary, respectively. The boundaries in the ionosphere and magnetosphere are connected by geomagnetic field lines, which are partly visualized with the semi-transparent surfaces.

Figure 1.

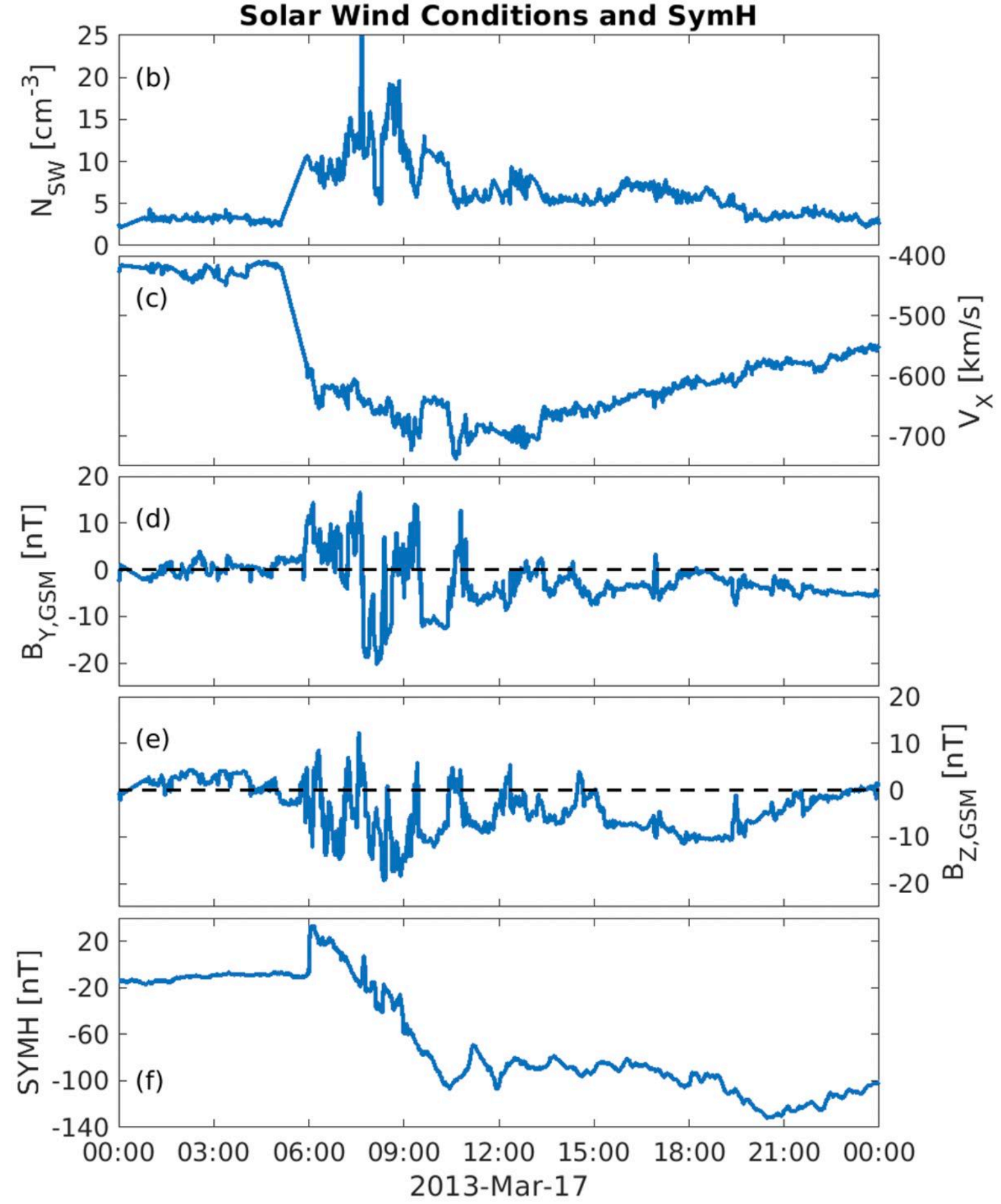
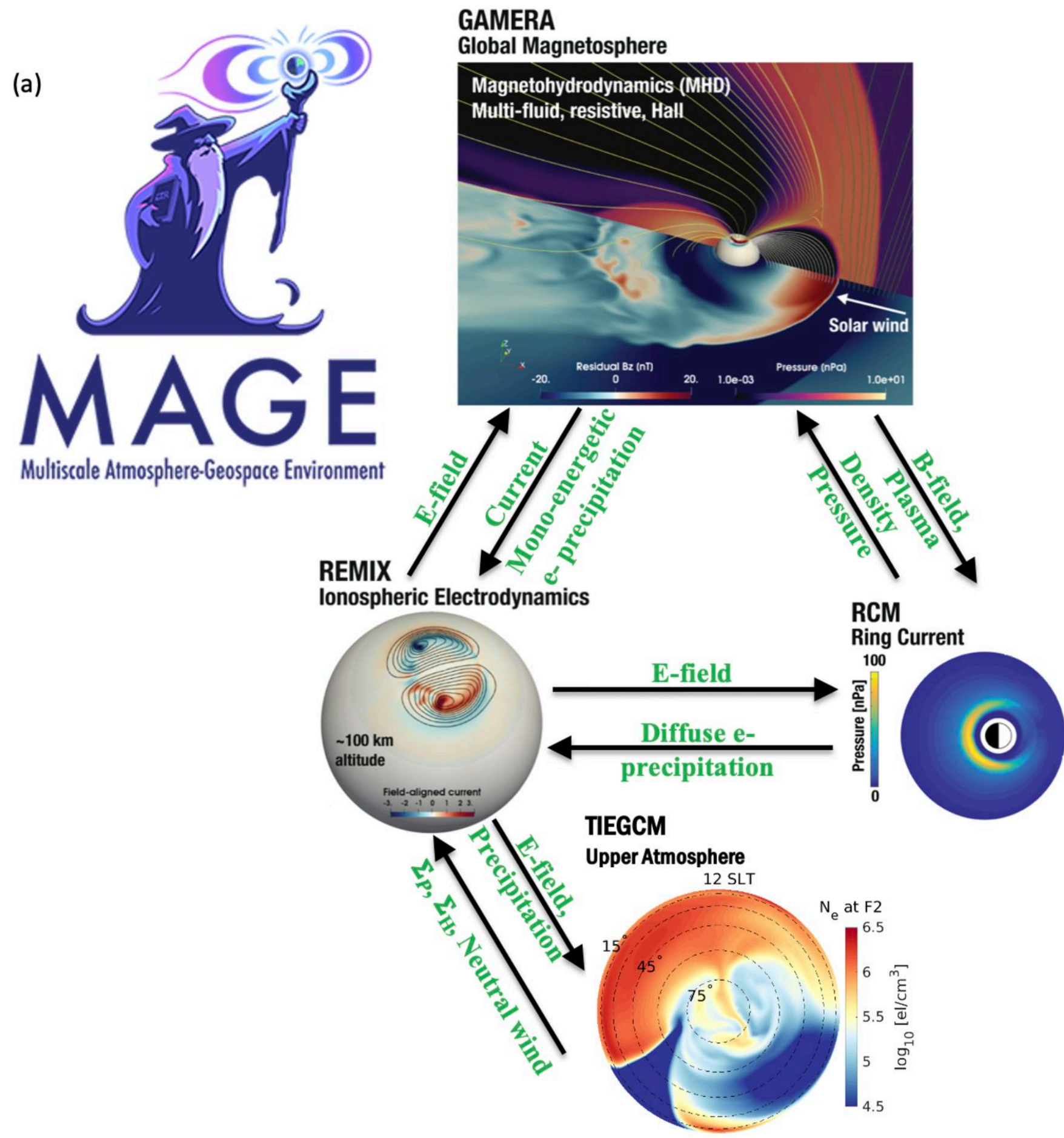


Figure 2.

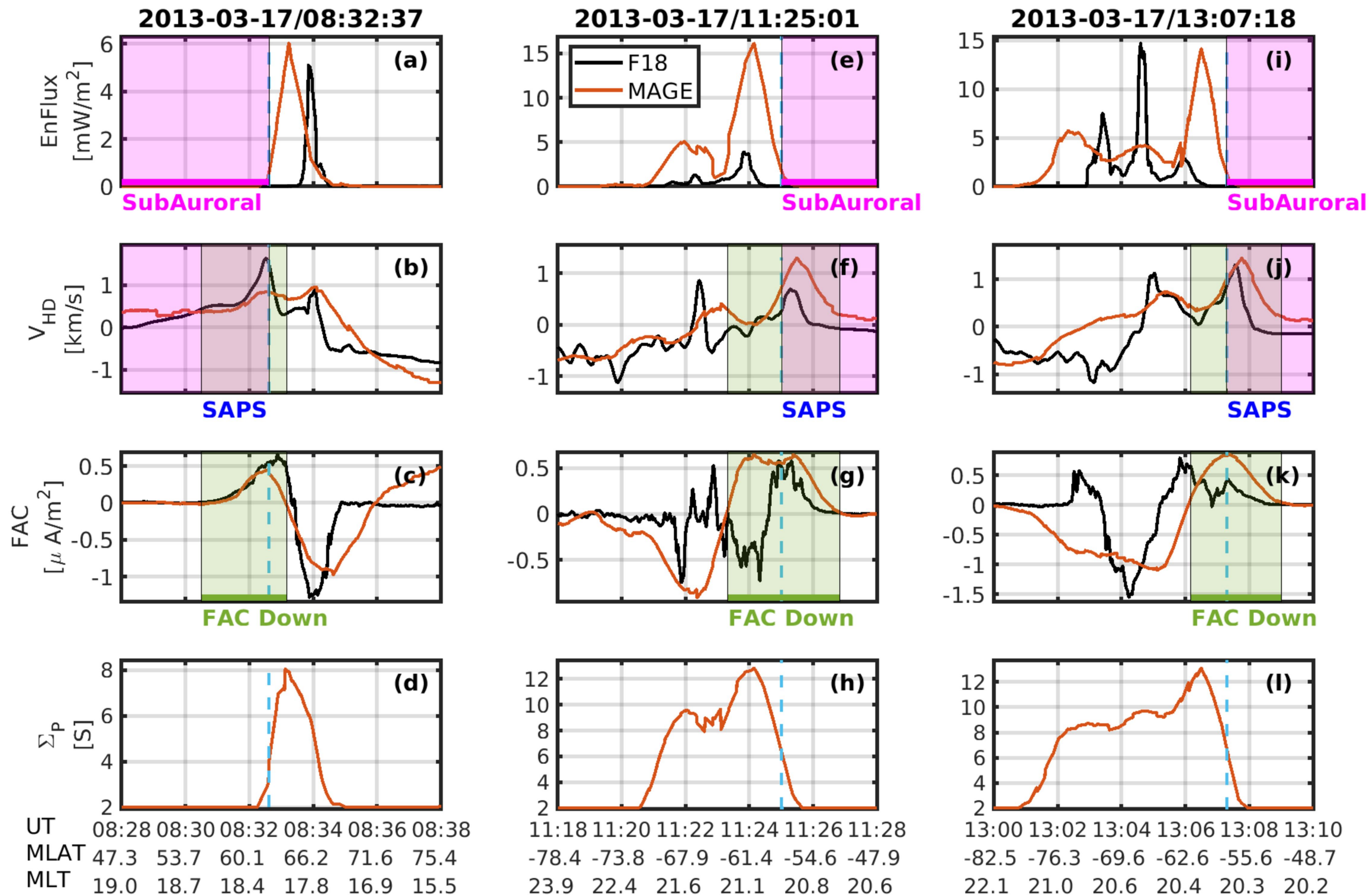
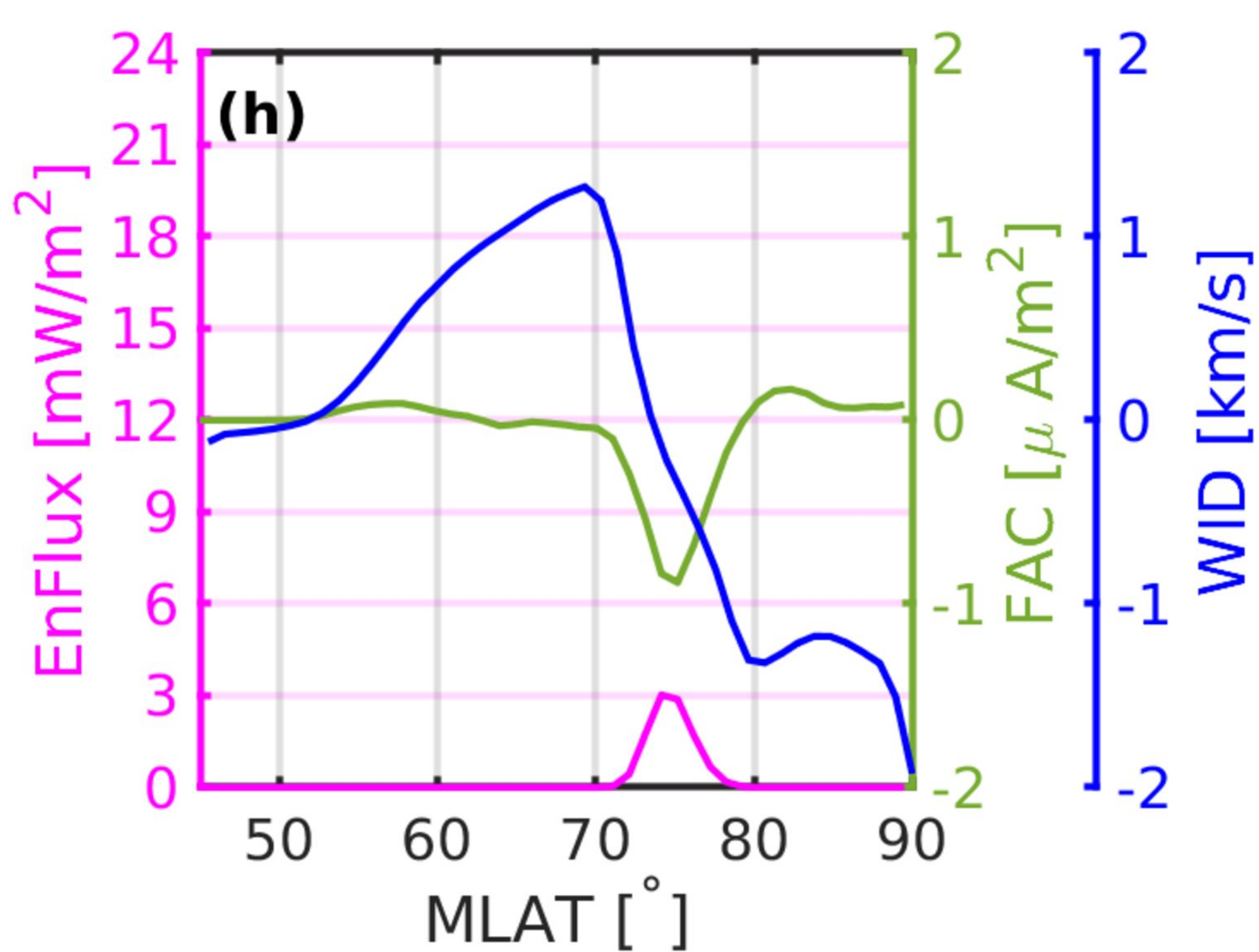
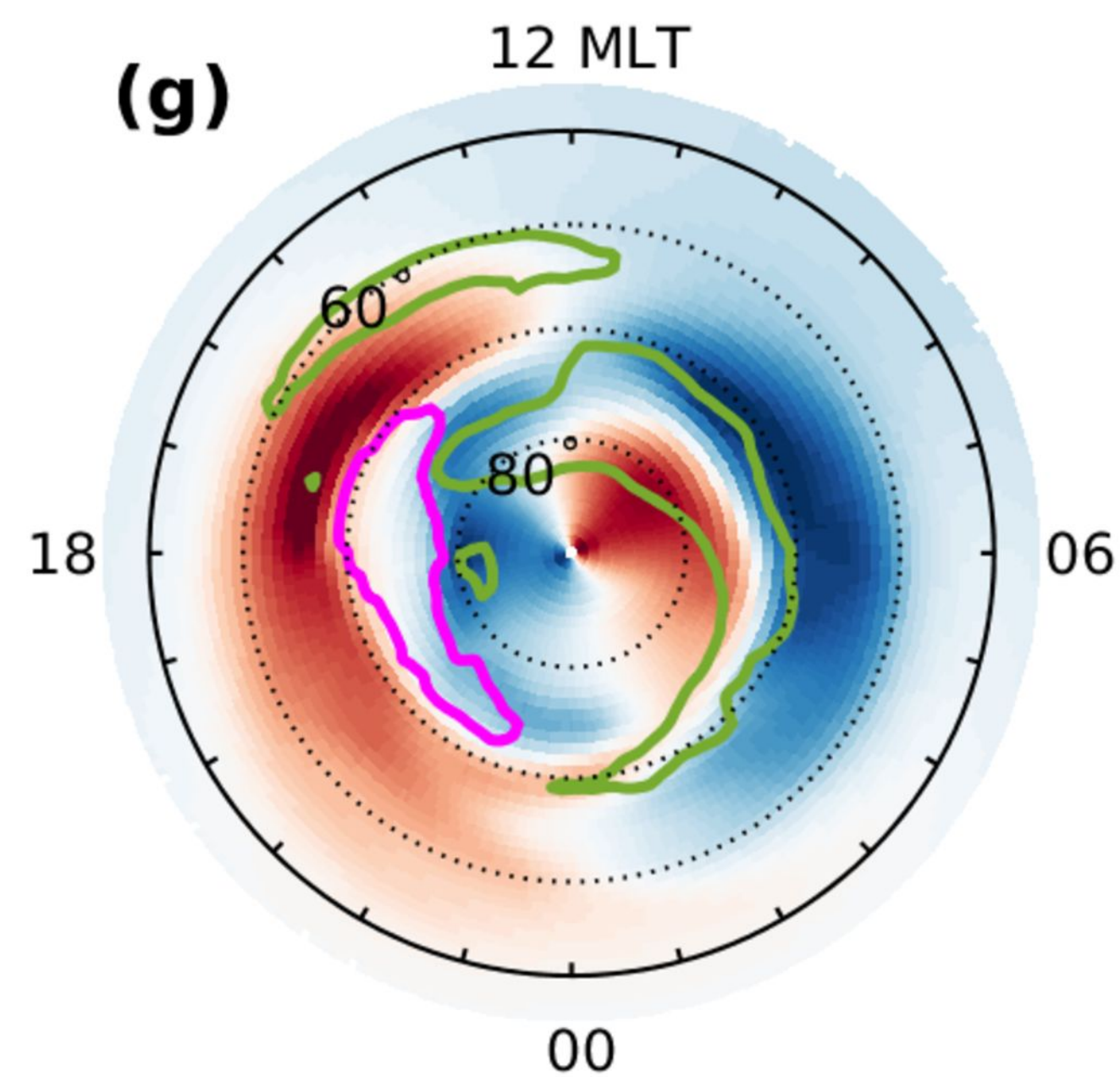
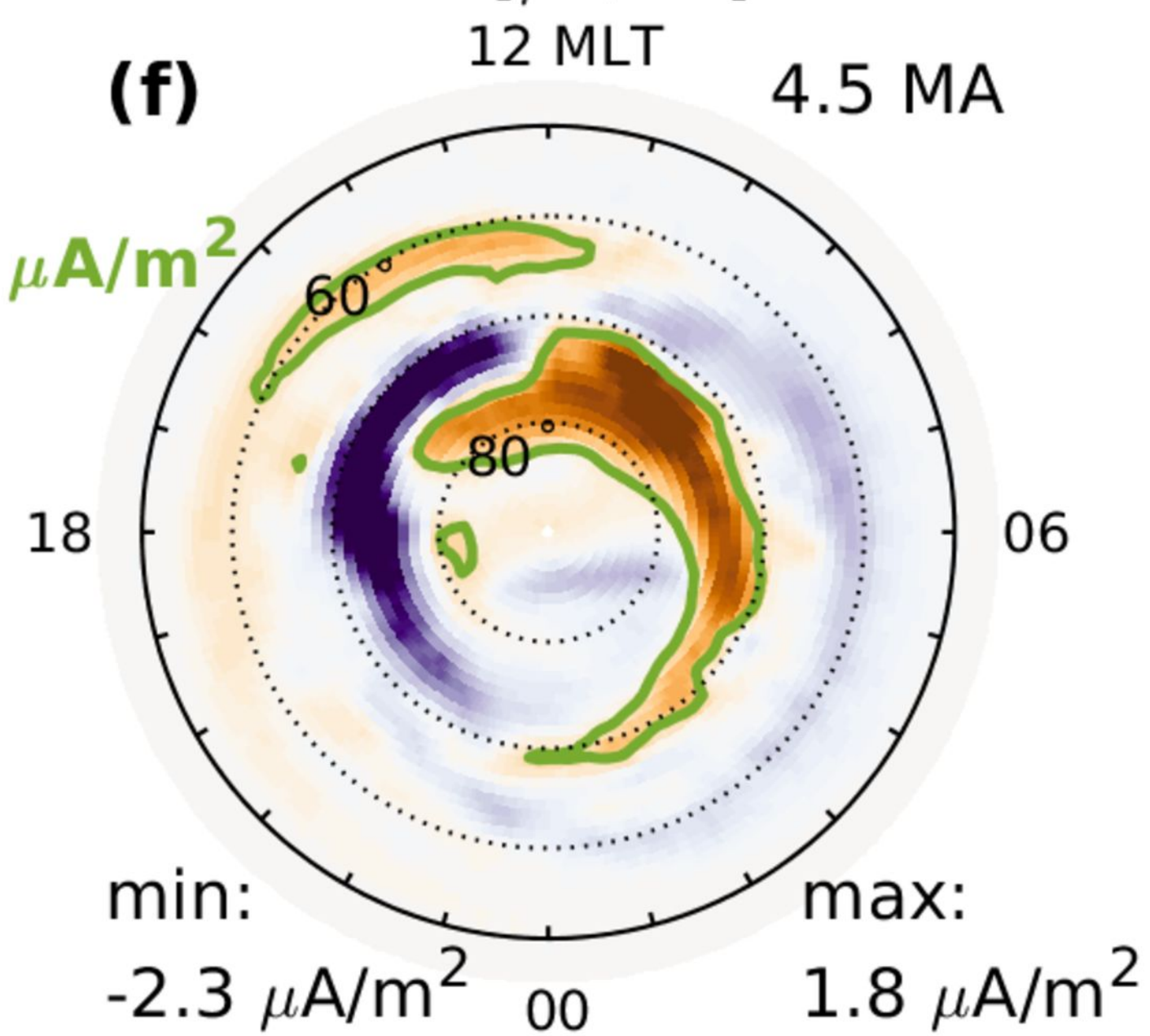
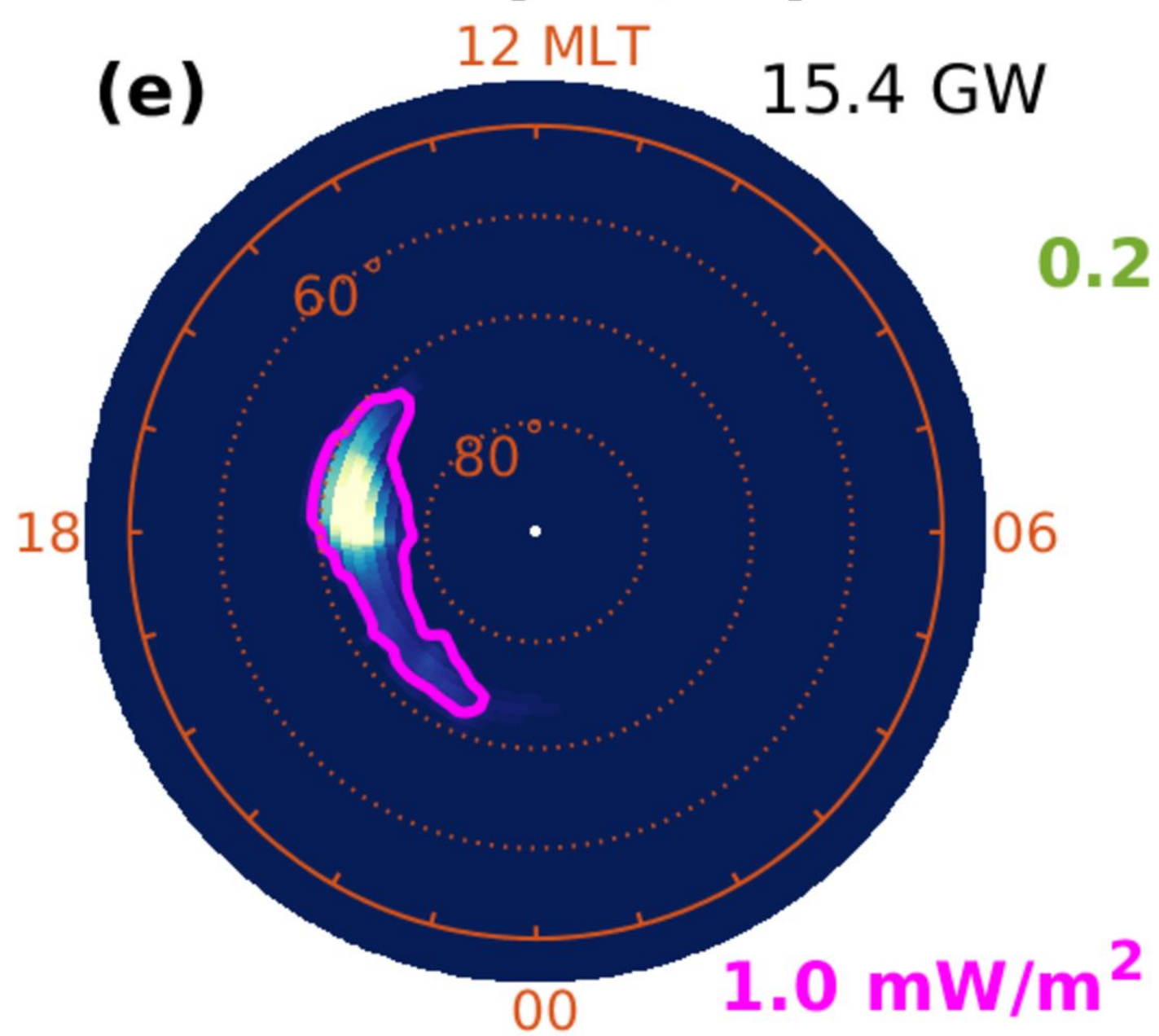
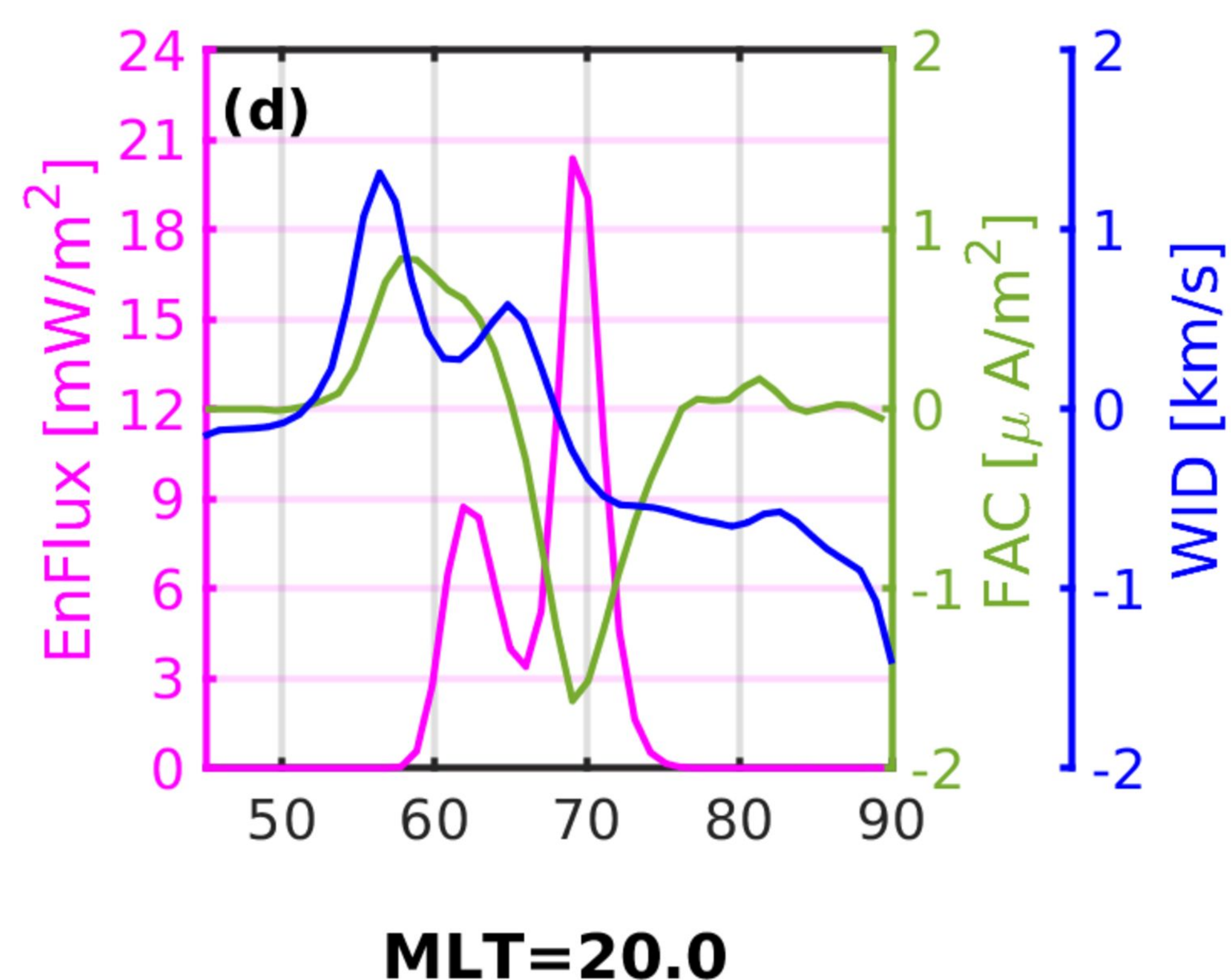
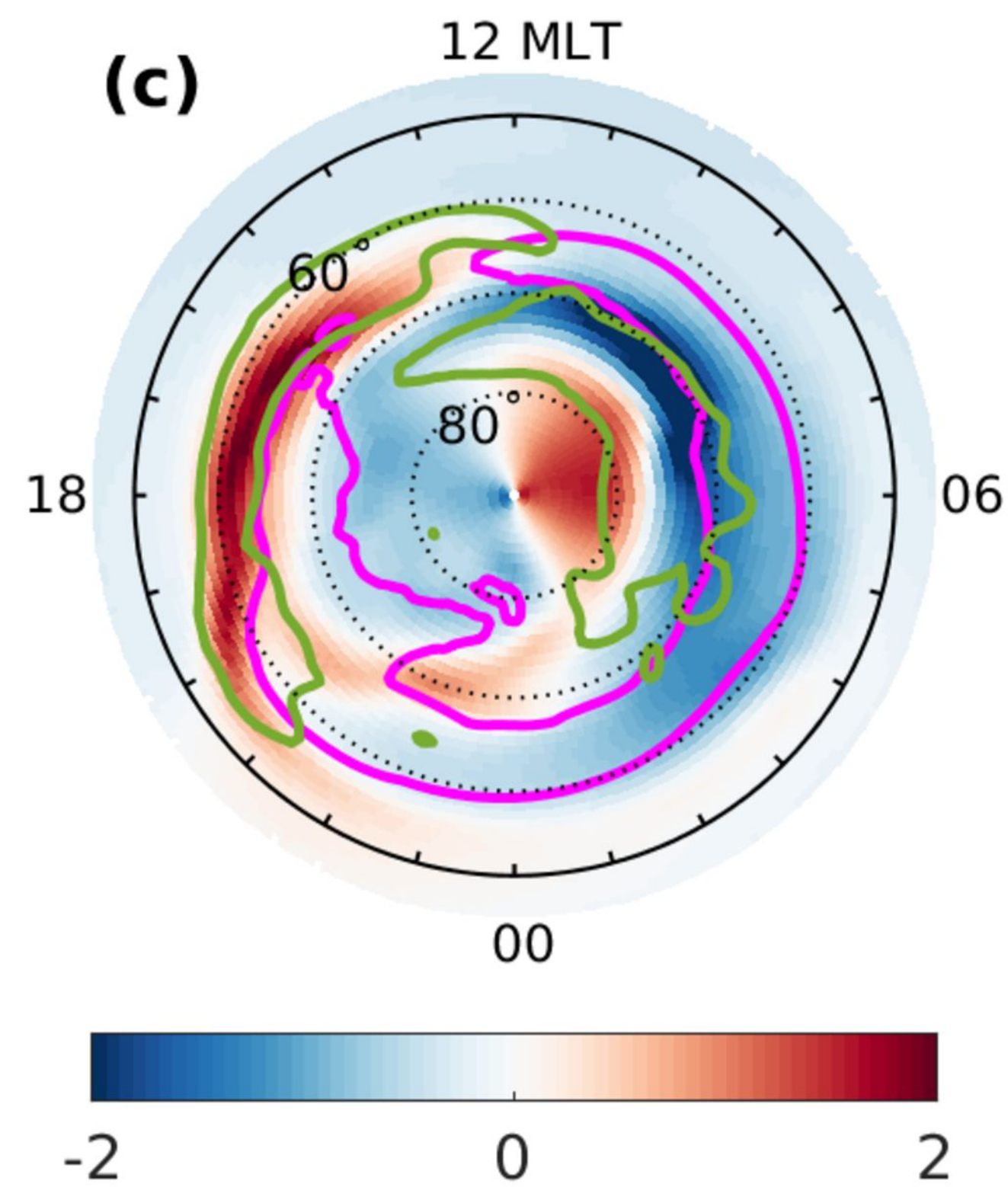
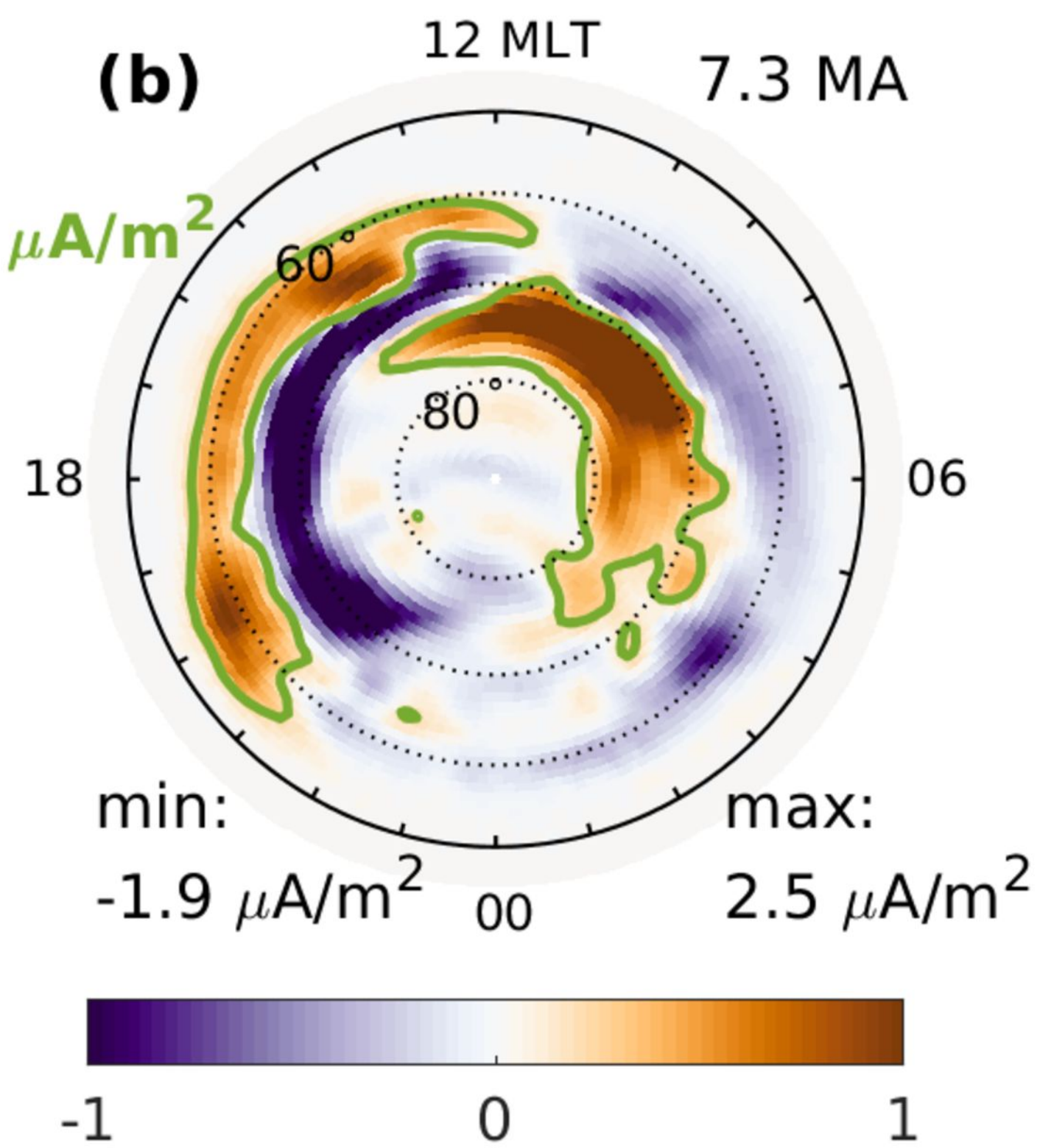
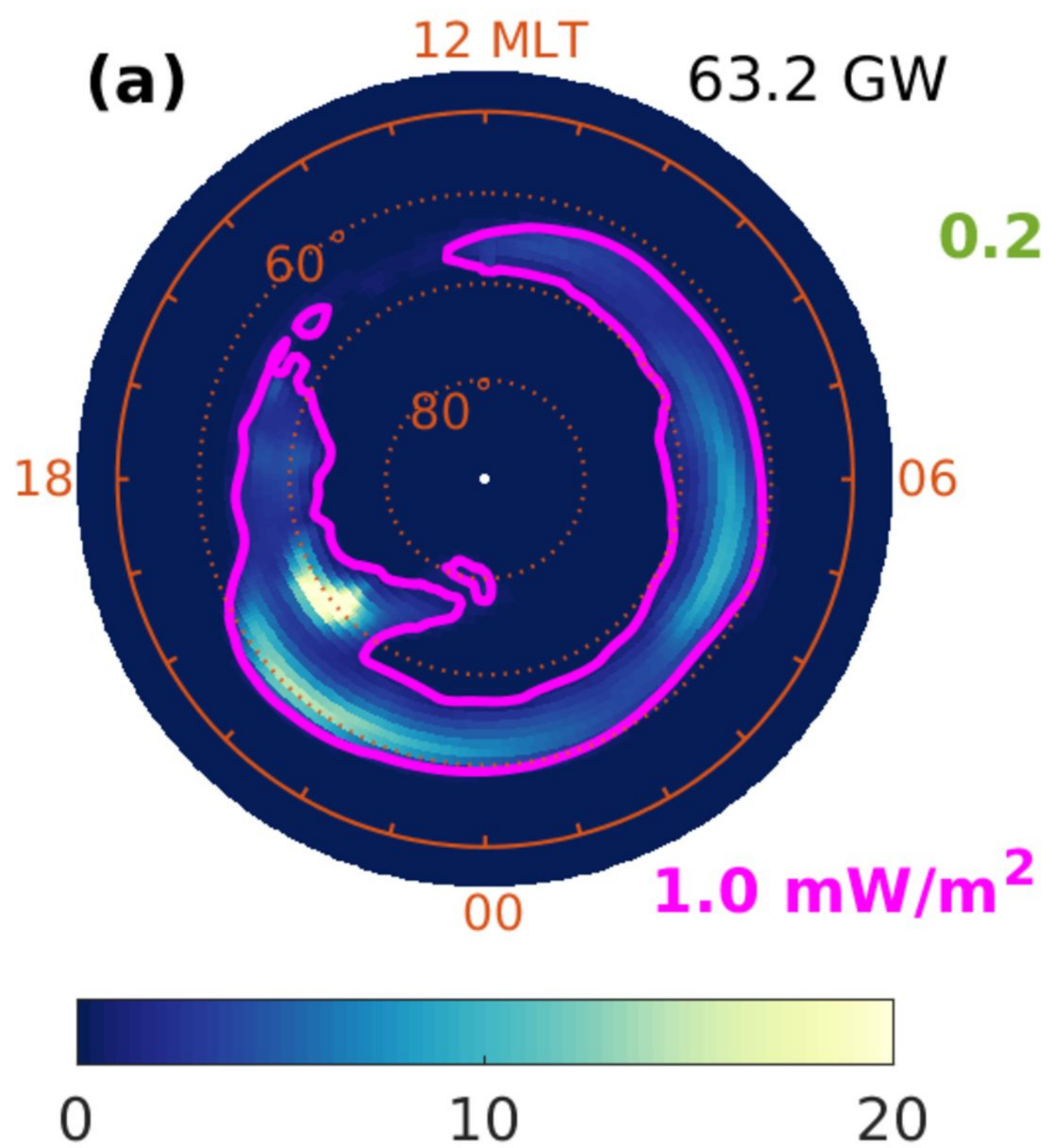
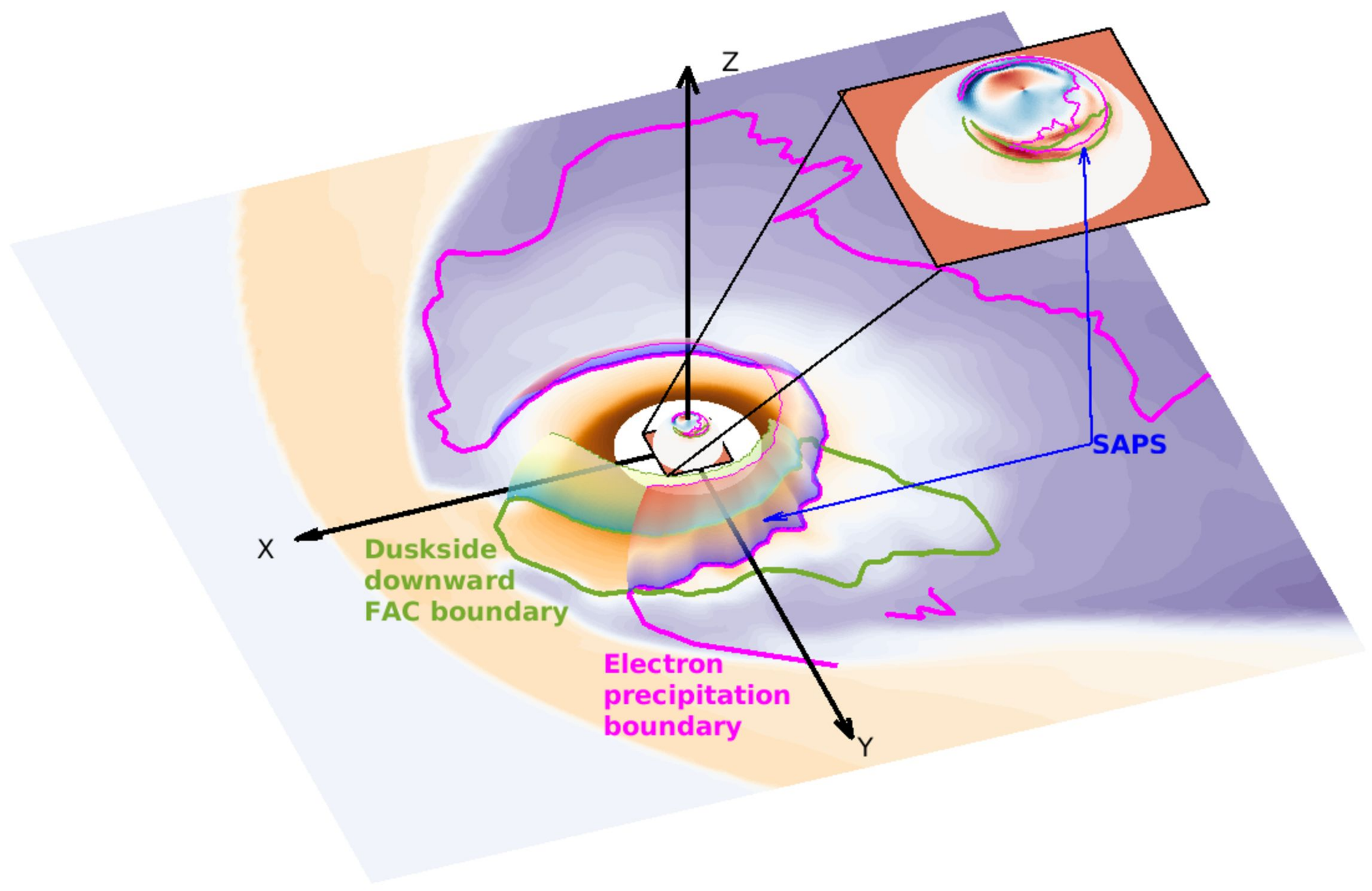


Figure 3.

2013-03-17T11-10-00



**Figure 4.**



**The role of diffuse electron precipitation in the formation of subauroral polarization streams**

Dong Lin<sup>1</sup>, Kareem Sorathia<sup>2</sup>, Wenbin Wang<sup>1</sup>, Viacheslav Merkin<sup>2</sup>, Shanshan Bao<sup>3</sup>, Kevin Pham<sup>1</sup>,  
Frank Toffoletto<sup>3</sup>, Xueling Shi<sup>4</sup>, Adam Michael<sup>2</sup>, John Lyon<sup>5</sup>, Jeffrey Garretson<sup>2</sup>, and Brian  
Anderson<sup>2</sup>.

<sup>1</sup>High Altitude Observatory, National Center for Atmospheric Research, Boulder CO,

<sup>2</sup>Applied Physics Laboratory, Johns Hopkins University, Laurel MD,

<sup>3</sup>Department of Physics and Astronomy, Rice University, Houston TX,

<sup>4</sup>Bradley Department of Electrical and Computer Engineering, Virginia Tech, Blacksburg VA,

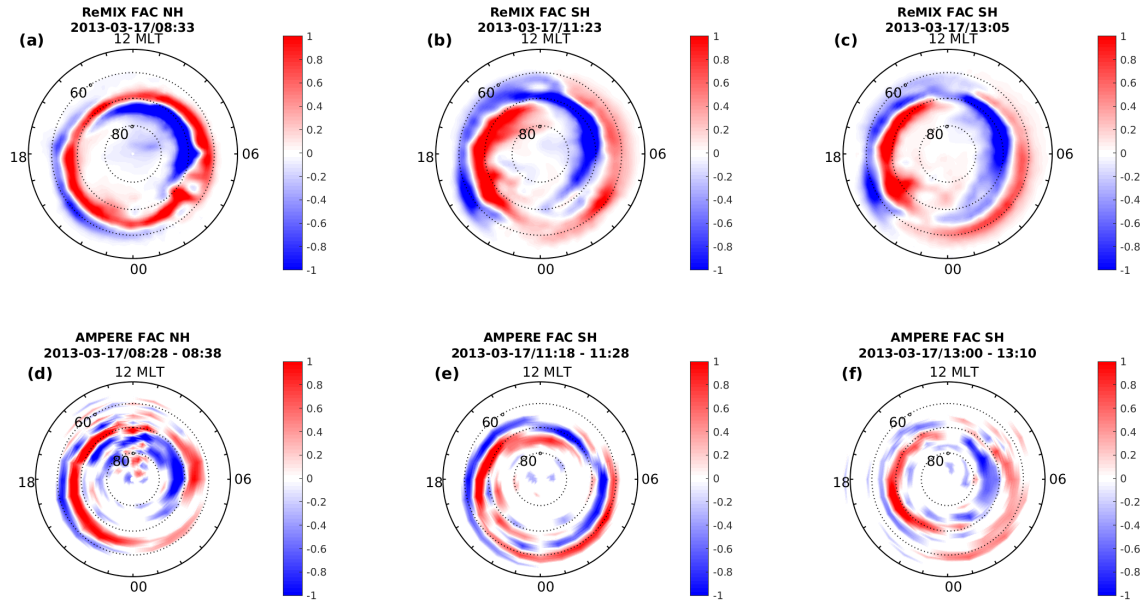
<sup>5</sup>Department of Physics and Astronomy, Dartmouth College, Hanover NH

**Contents of this file**

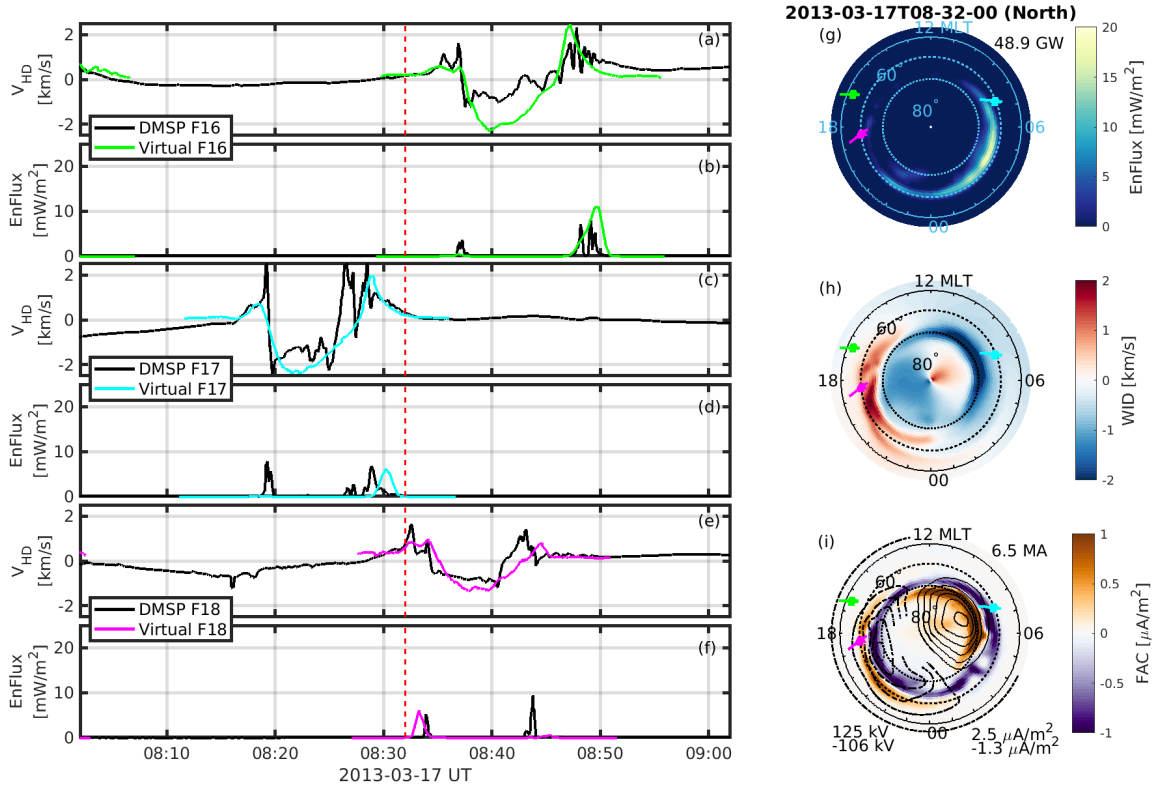
1. Figures S1.
2. Caption for Movie S1.

**Introduction**

This supporting information provides Figure S1 and caption for Movie S1 to show additional data-model comparison between the MAGE simulation results and AMPERE/DMSF measurements.



**Figure S1.** Comparison of field-aligned current (FAC) from MAGE/REMIX modeling results (top row) and AMPERE measurements (bottom row). Upward currents are shown in red and downward currents in blue. The REMIX FACs are output in the middle of the three 10-min intervals shown in Figure 2. The AMPERE FACs are fitted based on the corresponding 10-min measurements of magnetic perturbation. AMPERE data are available at <http://ampere.jhuapl.edu/>. The comparison shows that the simulated FACs are close to the AMPERE fitted FAC in terms of the spatial coverage and location of the large scale FAC structures.



**Movie S1.** A movie showing the comparison between MAGE simulation results and DMSP F16, F17, and F18 measurements. The plot above is one frame used to illustrate the format. The left column shows comparison of horizontal ion drifts ( $V_{HD}$ ) and integrated electron precipitation energy flux (EnFlux) from DMSP F16, F17, and F18 measurements (black for all real measurements), and MAGE simulation results sampled along the DMSP trajectories, namely virtual F16 (green), virtual F17 (cyan), and virtual F18 (magenta). The red vertical dashed line indicates 11:25 UT, at which time the two-dimension distributions of EnFlux, westward ion drifts (WID), and field-aligned currents and electrostatic potential are shown in the right column. The locations of DMSP F16, F17, and F18 satellites are indicated by the green, cyan, and magenta arrows in the right column. Plots of similar format are combined in Movie S1.